scientific reports

Check for updates

OPEN

An investigation of the mechanical properties and adsorption potentials of Fe_2O_3@SiO_2-L-cysteine-cellulose system

Mehdi Khalaj[1]✉ & Majid Ghashang[2]

In this study, the Fe_2O_3@SiO_2-L-cysteine-cellulose system was synthesized and characterized through XRD, FT-IR, EDS, and TGA-DTA analyses. This system's adsorption performance was evaluated for removing heavy metals such as Cr, Cd, Ni, and Pb from synthetic wastewater. The magnetic core demonstrated a beneficial effect on enhancing the metal adsorption capacity of the polymer, while the magnetic properties facilitated the recyclability of the adsorbent. The adsorption of Cr(VI), Cd(II), Ni(II), and Pb(II) ions was explored under varying conditions of pH, temperature, metal ion concentration, and adsorbent dosage. Maximum adsorption capacities for Cd(II), Ni(II), and Pb(II) ions were recorded at 423.56 mg/g, 426.32 mg/g, and 422.21 mg/g, respectively, under optimal conditions of pH 6.5, metal ion concentration of 600 mg/L, an adsorbent dose of 0.07 g, and room temperature. Additionally, the adsorption capacity of the material for water, N_2, and CO_2 was assessed. The system exhibited excellent removal efficiency for Cr(VI) ions (˃98%) at an initial Cr(VI) concentration of 90 mg/L using 0.07 g of the adsorbent. The combination of Fe_2O_3@SiO_2, L-cysteine, and cellulose in one adsorbent system performs distinct advantages for heavy metal adsorption such as enhanced surface area of adsorbent, preventing degradation in harsh conditions, magnetic separation and reusability of the adsorbent.

Keywords Wastewater, Cellulose, Fe_2O_3@SiO_2- L-cysteine -cellulose system, CO_2 adsorption, Heavy metals, Adsorption

Carbohydrate polymers can be extracted from various plant and animal sources. Thus, scientists and researchers can easily, safely, and cheaply access such polymers, which is why they are always used for various industrial and laboratory applications. In the meantime, what increases the importance of these polymers is the modification of their structure, and many modified structures of carbohydrate polymers have been used in industrial and laboratory applications[1,2].

Cellulose is one of the polymers that can be used in various forms such as fibers, nanoparticles, and nanocrystals as a drug carrier and as a water-separating system from oil as well as the absorbent of heavy metals and different gases. Cellulose has been created as a base for various adsorbents, suitable levels, good mechanical stability, and excellent biocompatibility. Due to its ability to be chelated with metals and accessible hydroxyl groups, cellulose can be used as a good candidate for absorbing heavy metal ions. One of the remarkable points about cellulose-based absorbents is the possibility of their decomposition in natural processes, so their residues are not considered environmental pollutants. The main challenge in using cellulose as an adsorbent is the ability of chelating hydroxyl groups in cellulose to absorb heavy metals, which does not meet researchers' expectations. Therefore, there is a need to create a suitable framework or architecture to solve the challenges of cellulosic adsorbents[3–8].

Nanocellulose-based adsorbents have emerged as sustainable and effective materials for removing heavy metal ions. To enhance the adsorption capabilities of nanocellulose, several modification techniques have been explored. Simple and affordable methods, such as functionalization and cross-linking, have proven particularly useful in improving the surface properties of cellulose. Cross-linking can involve the addition of different functional groups, such as carboxyl, sulfo, and amino groups. Among these, amino groups offer the most promise for enhancing adsorption performance due to their strong metal ion binding properties[7,9–12].

[1]Department of Chemistry, Buinzahra Branch, Islamic Azad University, Buinzahra, Iran. [2]Department of Chemistry, Najafabad Branch, Islamic Azad University, NajafabadP.O. Box: 517, Iran. ✉email:

With the rise of industrialization and the rapid expansion of industrial processes, heavy metals have increasingly contaminated natural environments and water bodies, including groundwater, rivers, lakes, and oceans. Unlike organic pollutants, heavy metals are not biodegradable and cannot be naturally recycled, posing long-term risks to ecosystems and human health if left untreated. This has led to widespread recognition of the need to prevent heavy metal contamination and to decontaminate polluted water sources. In reviewing approaches to heavy metal removal, several key techniques have been identified, such as chemical precipitation, adsorption, electrochemical reduction, coagulation and flocculation, membrane filtration, reverse osmosis, and ion exchange. Although these methods can effectively remove heavy metals, challenges remain, including high costs, the need for advanced equipment, potential secondary pollution, and limited efficiency in certain cases[13–18].

Among the presented methods, the absorption method has gained a higher scope due to the possibility of using different adsorbents and also optimizing the structure of the existing adsorbents. The use of adsorbents with high absorption capacity has introduced the absorption technique as a reliable method with good efficiency. The main challenge of the absorption technique can be found in the recyclability of the adsorbents, the complex process for preparation, as well as the high cost of the adsorbents. In normal processes, adsorbents can be separated and recycled using centrifugation or simple filtration methods. These methods, with significant waste of adsorbent, practically limit the recycling of adsorbent and prevent their widespread and practical applications in water purification. A practical solution to these challenges is using magnetic absorbent materials[19–29]. Magnetic absorbers have an easy and affordable separation process and are recycled with the help of an external magnet. Most of the magnetic absorbents are made based on hematite and magnetite. The main challenge in using these compounds is their tendency to agglomerate and lack of stability in acidic environments. The use of polymer coatings and the formation of core-shell structures of these compounds to modify the magnetic particles and improve their absorption properties is one of the most popular methods used in recent years[30–46].

This research aimed to examine the adsorption performance of a Fe_2O_3@SiO_2-L-cysteine-cellulose composite for removing Cr(VI), Cd(II), Ni(II), and Pb(II) heavy metal ions, along with water, nitrogen (N_2), and carbon dioxide (CO_2) gases. The study focused on understanding the effects of various experimental conditions on the adsorption efficiency and capacity of the developed adsorbent system.

The Fe_2O_3@SiO_2-L-cysteine-cellulose system combines Fe_2O_3, silica, L-cysteine, and cellulose to offer notable advantages for heavy metal adsorption. Fe_2O_3 increases surface area and imparts magnetic properties, facilitating easy recovery and reuse of the adsorbent. The silica coating enhances the material's stability, preventing degradation under harsh conditions. L-cysteine functionalization introduces sulfur groups that improve the adsorption of metal ions, especially Pb(II) and Cd(II). Although cellulose is widely used for metal removal, the novelty of this work lies in the synergistic combination of magnetic separation, structural stability, and functionalization, which significantly enhances performance and reusability.

Experimental

Reagents and instrumentation

All chemicals used in this study were obtained from Merck and Sigma-Aldrich. The following instruments were employed: X-ray Diffraction (XRD): A Shimadzu XRD device (model 6100, Cu-Kα irradiation) was used to investigate crystallinity and determine phases. Operating conditions were 40 kV and 30 mA, with a 2θ° range of 10–90. The sample storage chamber was made of aluminum, and a copper lamp (kα = 1.5418 nm) was used. Data collection occurred at a rate of 10°/min with 0.04° steps. Phases and components were identified by comparing diffraction peaks with standard cards using X'PertHighScore software. Absorption Spectrophotometer: Heavy metal concentrations were measured using a Shimadzu absorption spectrophotometer (model AA-6880). Thermogravimetric Analysis (TGA): Thermal behavior of the Fe_2O_3@SiO_2-L-cysteine-cellulose system was analyzed using a Shimadzu TGA-DTG-60 H instrument. Fourier Transform Infrared Spectroscopy (FT-IR): FT-IR analysis was conducted on a Bruker IR spectrophotometer, using a KBr disk within a range of 400 to 4000 cm^{-1}. Field Emission Scanning Electron Microscopy (FE-SEM) and Energy Dispersive X-ray Spectroscopy (EDX): Morphology and chemical composition of the adsorbent were examined with a JEOL JSM-IT 100 instrument.

Preparation of Fe2O3@SiO2-L-cysteine -cellulose system

Step 1: preparation of intermediate A

Figure 1 provides an overview of the process for synthesizing the Fe_2O_3@SiO_2-L-cysteine-cellulose composite. The Fe_2O_3@SiO_2 was produced following the method outlined in previous research[47]. In a 250 mL flask, 25 mmol of (3-chloropropyl)trimethoxysilane and 25 mmol of L-cysteine were dissolved in 100 mL of toluene and refluxed overnight. After that, 20 g of Fe_2O_3@SiO_2 nanoparticles were added to the solution, stirred, and refluxed for an additional 24 h. The solid was then separated, washed with toluene, and dried at 50 °C (as shown in Fig. 1). The product was characterized using XRD, EDX, and FTIR analyses.

Step 2: synthesis of intermediate B

In this step, 10 g of cellulose was dissolved in 100 mL of brine in a 250 mL flask. Then, 8 g of $NaIO_4$, dissolved in 50 mL of water, was added, and the mixture was heated to 50 °C with stirring for 10 h. Afterward, 1 mL of ethylene glycol was introduced and stirred for another 2 h at room temperature. The mixture was filtered, rinsed with deionized water, and dried under a vacuum.

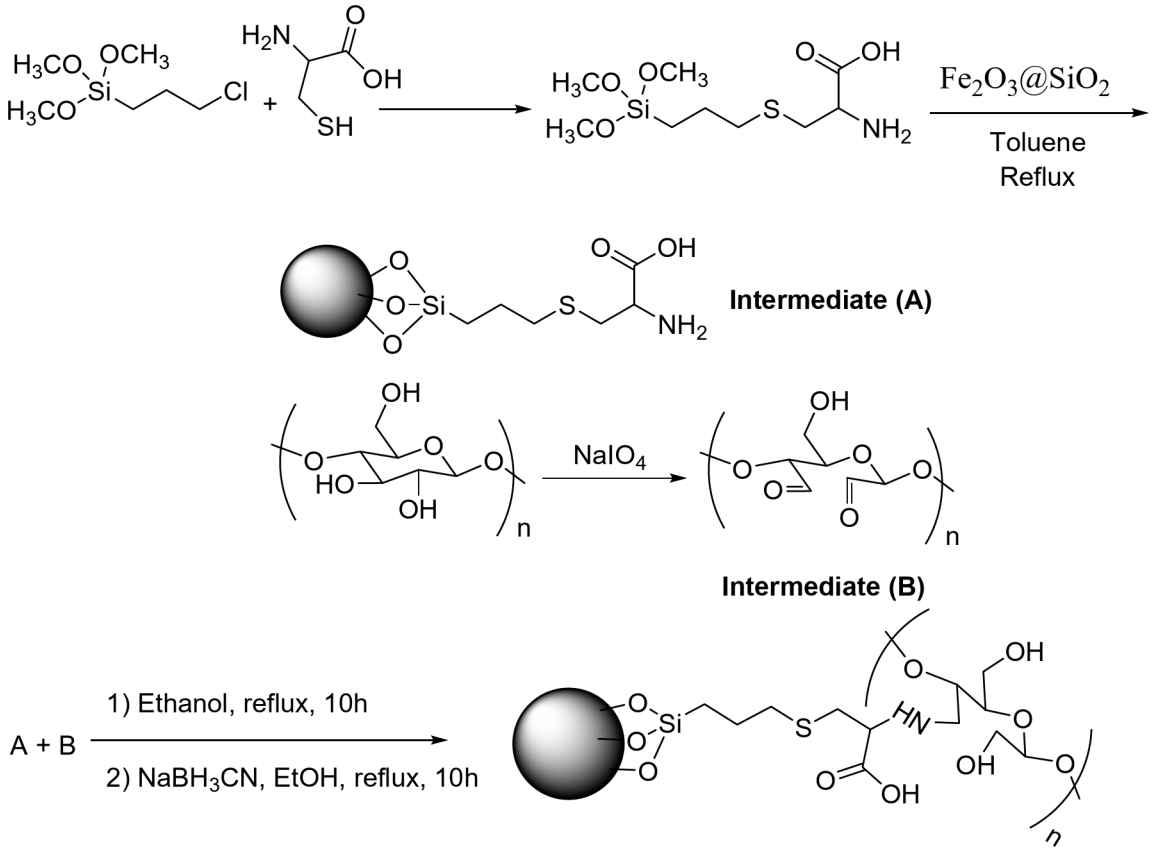

Fig. 1. Schematic preparation of Fe_2O_3@SiO_2-L-cysteine -cellulose system.

Step 3: assembly of the Fe_2O_3@SiO_2-L-cysteine-cellulose composite
The prepared samples from steps A and B (5 g each) were combined in 100 mL of ethanol and heated to 80 °C with stirring for 5 h. Next, 10 mmol of $NaBH_3CN$ dissolved in ethanol was added, and the reaction mixture was refluxed for 24 h. The final product was filtered and washed with ethanol and water.

Adsorption experiment For metal ion solutions, specific amounts of $Na_2Cr_2O_7.2H_2O$ (for Cr(VI)), $Cd(NO_3)_2.6H_2O$ (for Cd(II)), $Ni(NO_3)_2.6H_2O$ (for Ni(II)), and $Pb(NO_3)_2.6H_2O$ (for Pb(II)) were dissolved in 100 mL of deionized water, yielding solutions with concentrations of 100, 250, 500, 650, 750, and 850 mg/L. The pH of these solutions was adjusted between 3 and 8 using 1 M NaOH and 1 M HCl to investigate the pH effect on adsorption.

Adsorption procedure In a 250 mL Erlenmeyer flask, 0.6 g of the Fe_2O_3@SiO_2-L-cysteine-cellulose composite was mixed with 50 mL of heavy metal ion solutions, each with an initial concentration of 500 mg/L. The mixture was stirred at room temperature for 60 min. After filtration, the clear solution was collected and preserved for analysis using atomic absorption spectroscopy. To evaluate the adsorption process, the impact of several parameters was examined, including pH levels (3 to 8), concentrations of Cd(II), Ni(II), and Pb(II) (100–850 mg/L), the amount of adsorbent used (0.1–1 g), and temperature variations (25 to 70 °C).

The adsorption capacity at equilibrium (qe) was determined based on the following variables:

$q_e = \frac{(C_0 - C_e)V}{m}$ $q_t = \frac{(C_0 - C_t)V}{m}$

C0: Initial concentration (mg/L).
Ce: Equilibrium concentration (mg/L).
m: Mass of the adsorbent (g).
V: Volume of the solution (L).
q_t: Adsorption capacity at a given time t.

Results and discussion

Characterization of Fe2O3@SiO2-L-cysteine-cellulose system

To confirm the successful preparation of the Fe_2O_3@SiO_2-L-cysteine-cellulose composite, as illustrated in Fig. 1, the formation of bonds, phase characteristics, and chemical composition of intermediates A and the final composite were evaluated using FT-IR, XRD, and EDS techniques. Figure 2 displays the FT-IR spectra for Fe_2O_3@SiO_2, intermediate A, and the Fe_2O_3@SiO_2-L-cysteine-cellulose composite. The FT-IR spectrum for the Fe_2O_3@SiO_2 sample shows stretching vibrations associated with Si-OH and Si-O-Si bonds at 1673, 930,

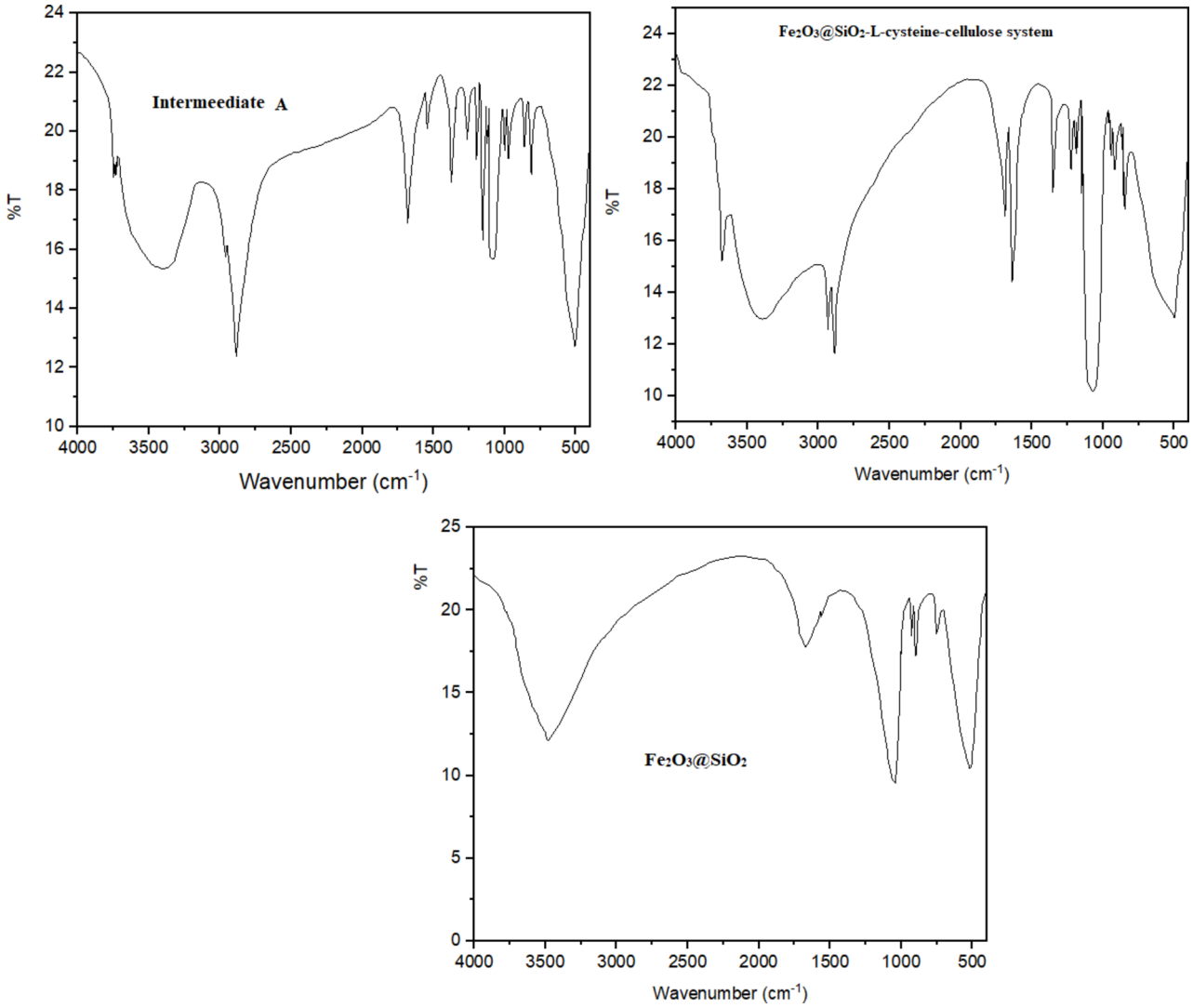

Fig. 2. FT-IR analysis of Fe_2O_3@SiO_2, Intermediate **A**, and Fe_2O_3@SiO_2-L-cysteine-cellulose system.

and 898 cm^{-1}, along with a Fe-O bond at 508 cm^{-1}, and bending vibrations for O-Si-O at 1065 cm^{-1}. After the introduction of L-cysteine, new stretching vibrations appeared, including those for O-H (broad peak between 3200 and 3600 cm^{-1}), N-H (at 3743 cm^{-1}), and C-H (sp^3, at 2881 cm^{-1}), along with COO (at 1685 cm^{-1}), C-C (at 1544 cm^{-1}), and bending vibrations for H-C-H (at 1373 cm^{-1}). These changes indicate that the structure of Fe_2O_3@SiO_2 has been effectively modified. When comparing the FT-IR spectra of Fe_2O_3@SiO_2 and intermediate A with that of the Fe_2O_3@SiO_2-L-cysteine-cellulose composite, the latter displays additional stretching vibrations corresponding to acetal groups from the cellulose chain at 1678 cm^{-1}, along with a distinct peak at 1065 cm^{-1} linked to C-O bonds, which further supports the successful synthesis of the composite.

Figure 3 shows the XRD patterns of Fe_2O_3@SiO_2, intermediate A, and Fe_2O_3@SiO_2-L-cysteine-cellulose system. All patterns show an amorphous phase of silica by revealing a shoulder peak at 10–30 [2Θ°] and a rhombohedral phase of Fe_2O_3 with the characteristic peaks revealed at 33.2, 36.6, 41.2, 49.7, 54.2, 62.5, 64.5, and 72.0 [2Θ°] (Reference code: 00-001-1053). As can be seen, the modified samples of Fe_2O_3@SiO_2 (intermediate A, and Fe_2O_3@SiO_2-L-cysteine-cellulose system) have similar patterns but the intensity of peaks is reduced.

The EDS analysis was taken to investigate the chemical composition of the Fe_2O_3@SiO_2-L-cysteine-cellulose system (Fig. 4). As revealed, both samples composed of C, N, S, O, Fe, and Si elements and increasing of C and O percentages was done when intermediate **A** was converted to Fe_2O_3@SiO_2-L-cysteine-cellulose system.

Thermal stability of Fe2O3@SiO2-L-cysteine-cellulose system

The thermal stability and behavior of the Fe_2O_3@SiO_2-L-cysteine-cellulose composite were evaluated through TGA and DTA analyses, depicted in Fig. 5. The results indicate two main stages of decomposition. Initially, there is a weight loss of approximately 2%, which can be attributed to the evaporation of adsorbed water and the elimination of impurities. The first significant decomposition phase occurs between 200 and 250 °C, likely due to the release of CO_2 gas and a decarboxylation reaction. The second phase of weight loss, which takes place from 300 to 500 °C, is associated with the breakdown of the organic components within the sample. These

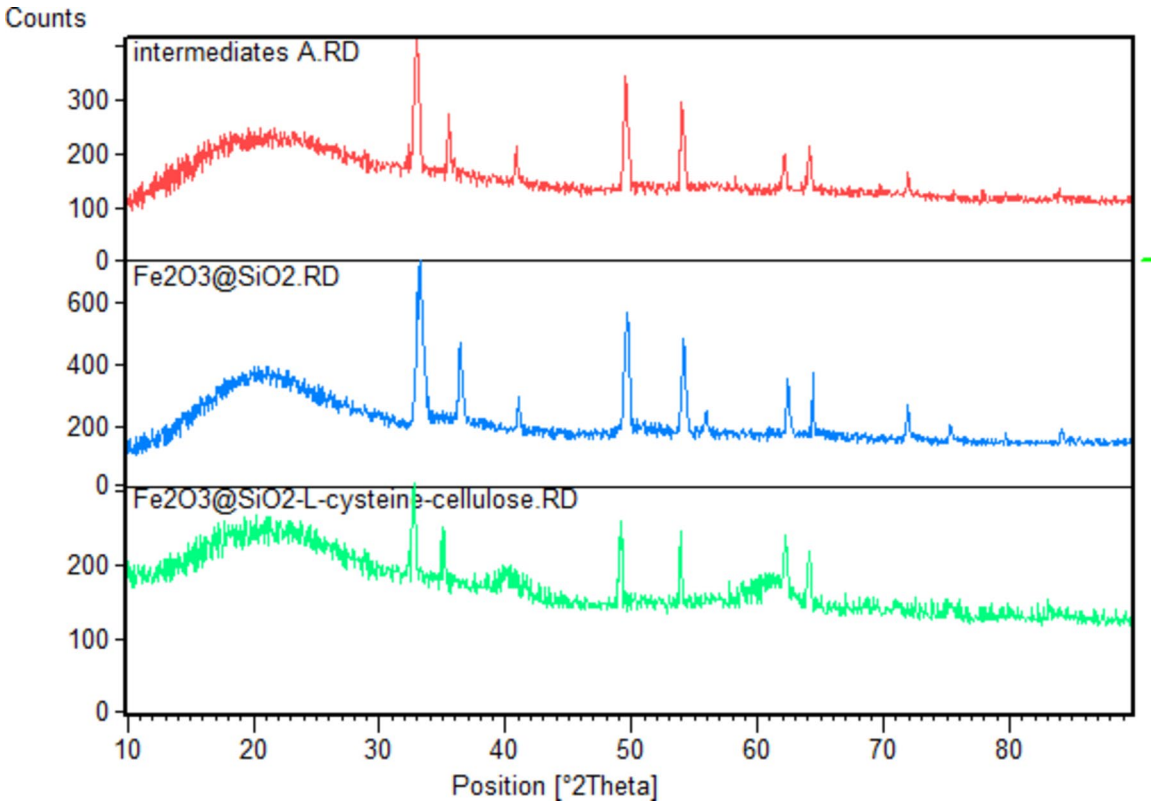

Fig. 3. XRD pattern of Fe_2O_3@SiO_2, Intermediate **A**, and Fe_2O_3@SiO_2-L-cysteine-cellulose system.

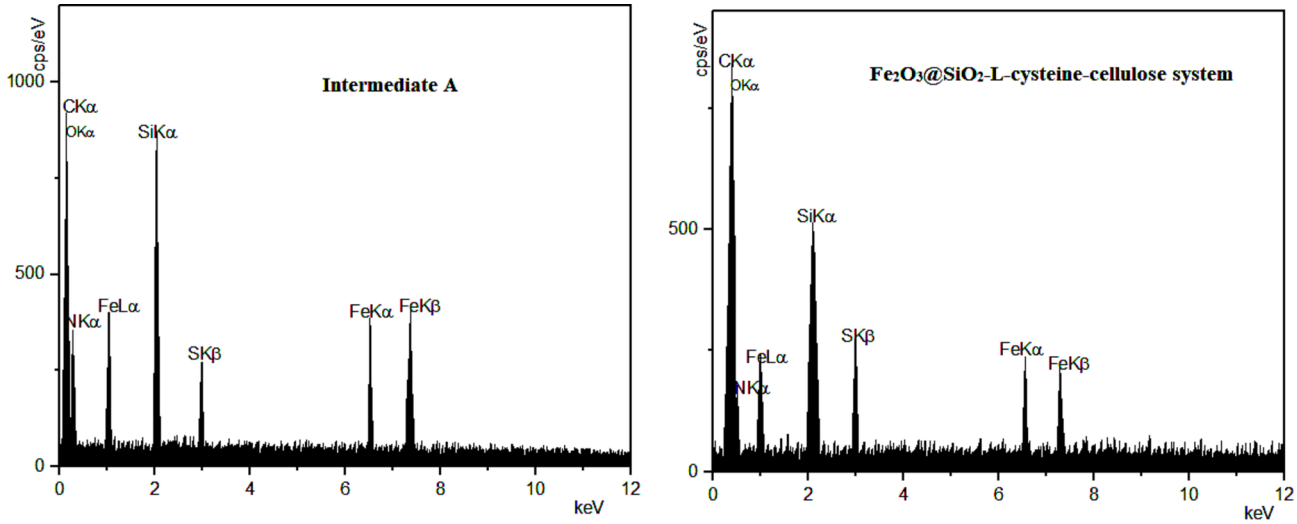

1 Date:9/22/2023 09:05:65 AM HV:25.0kV Puls th.:19.75kcps

El	AN	Series	unn. C [wt.%]	norm. C [wt.%]	Atom. C [at.%]	Error (1 Sigma) [wt.%]
O	8	K-series	44.21	42.11	57.48	5.97
C	6	K-series	6.82	6.21	11.12	0.81
Fe	26	K-series	20.65	19.01	7.37	0.65
N	7	K-series	1.64	1.22	1.85	0.03
Si	14	L-series	28.84	28.68	20.33	3.14
S	16	K-series	2.27	2.77	1.85	0.05
Total:			104.43	100.00	100.00	

2 Date:9/22/2023 3:07:51 PM HV:25.0kV Puls th.:18.70kcps

El	AN	Series	unn. C [wt.%]	norm. C [wt.%]	Atom. C [at.%]	Error (1 Sigma) [wt.%]
O	8	K-series	54.03	49.31	53.48	7.06
C	6	K-series	21.12	23.88	34.09	4.21
Fe	26	K-series	10.12	9.75	3.03	0.41
N	7	K-series	0.64	0.61	0.76	0.01
Si	14	L-series	11.84	15.04	7.88	1.14
S	16	K-series	1.27	1.41	0.76	0.02
Total:			99.02	100.00	100.00	

Fig. 4. EDS analysis of intermediate **A** and Fe_2O_3@SiO_2-L-cysteine-cellulose system.

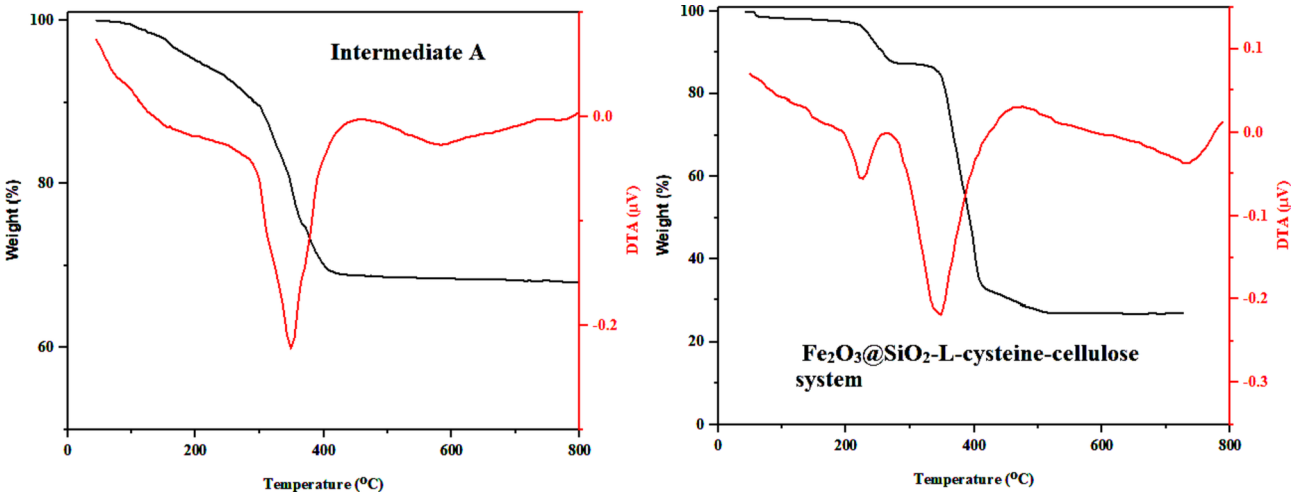

Fig. 5. TGA and DTA analysis of intermediate **A** and Fe_2O_3@SiO_2-L-cysteine-cellulose system.

TGA findings correspond well with the anticipated mass changes based on the materials used in the composite's preparation. In comparison, intermediate A shows a similar thermal decomposition pattern, with around 10% of its mass lost between 100 and 250 °C due to the removal of adsorbed water and impurities, along with CO_2 gas evolution during decarboxylation. A further mass loss observed from 250 to 400 °C is also linked to the degradation of organic materials.

VSM analysis of Fe2O3@SiO2-L-cysteine-cellulose system

Figure 6 illustrates the VSM analysis results for Fe_2O_3, intermediate A, and the Fe_2O_3@SiO_2-L-cysteine-cellulose system, conducted at 25 °C with a magnetic field range from − 10,000 to 10,000 Oe. The hysteresis curves in Fig. 6 reveal that the functionalization process significantly reduced key magnetic properties, including saturation magnetization (Ms), remanence magnetization (Mr), and coercivity field (Hc), as summarized in Table 1. Notably, Fe_2O_3 demonstrated robust magnetic characteristics, which were markedly diminished following functionalization. This reduction is attributed to the incorporation of the cellulosic chain, which exerts a diamagnetic influence that adversely affects the saturation magnetization. The diamagnetic nature of the organic chains in the Fe_2O_3@SiO_2-L-cysteine-cellulose system results in a considerable decrease in magnetic saturation when compared to both the pure Fe_2O_3 and intermediate A samples. This observation underscores the impact of organic functionalization on the magnetic properties of Fe_2O_3, highlighting a trade-off between enhanced functional attributes and magnetic performance.

Mechanical properties and water adsorption potential of Fe2O3@SiO2-L-cysteine-cellulose system

The mechanical properties of the Fe_2O_3@SiO_2-L-cysteine-cellulose system, including flexural strength (FS), flexural modulus (FM), and compressive strength (CS), were comprehensively evaluated and are detailed in Table 2. This composite exhibits significantly enhanced mechanical properties compared to intermediate A, highlighting its superior structural performance.

In addition to its mechanical robustness, the water adsorption capacity of the Fe_2O_3@SiO_2-L-cysteine-cellulose system was meticulously investigated, with findings depicted in Fig. 7. The composite demonstrates a high potential for water adsorption, attributed to the intrinsic hydrophilic nature of both the inorganic Fe_2O_3@SiO_2 particles and the organic L-cysteine-cellulose matrix. This dual-phase composition promotes substantial water uptake. Initially, the water adsorption rate is rapid and slows as the material approaches saturation, indicating an efficient and sustained adsorption process. These properties make the Fe_2O_3@SiO_2-L-cysteine-cellulose system an excellent candidate for applications requiring both high mechanical strength and significant moisture absorption capacity.

N_2 and CO_2 adsorption-desorption studies

The BET method was employed to evaluate the nitrogen adsorption potential of the Fe_2O_3@SiO_2-L-cysteine-cellulose system. Figure 8 displays the nitrogen adsorption-desorption isotherms, which are classified as type III according to the IUPAC standards. This classification confirms the system's high adsorption capacity and mesoporous structure, essential for various adsorption applications. Using both BET and BJH methods, key parameters such as specific surface area (SSA), pore volume, and pore diameter distribution were determined. The system exhibited an impressive SSA of 371.11 m^2/g, indicating a large surface area available for adsorption. Additionally, the pore diameter was found to be 17.32 nm, and the pore volume was measured at 0.048 cm^3/g. These values suggest that the Fe_2O_3@SiO_2-L-cysteine-cellulose system possesses a highly accessible mesoporous structure, making it a promising candidate for applications requiring efficient adsorption, such as in catalysis, separation processes, and environmental remediation. The substantial surface area and well-defined pore characteristics underscore its potential for high-performance adsorption.

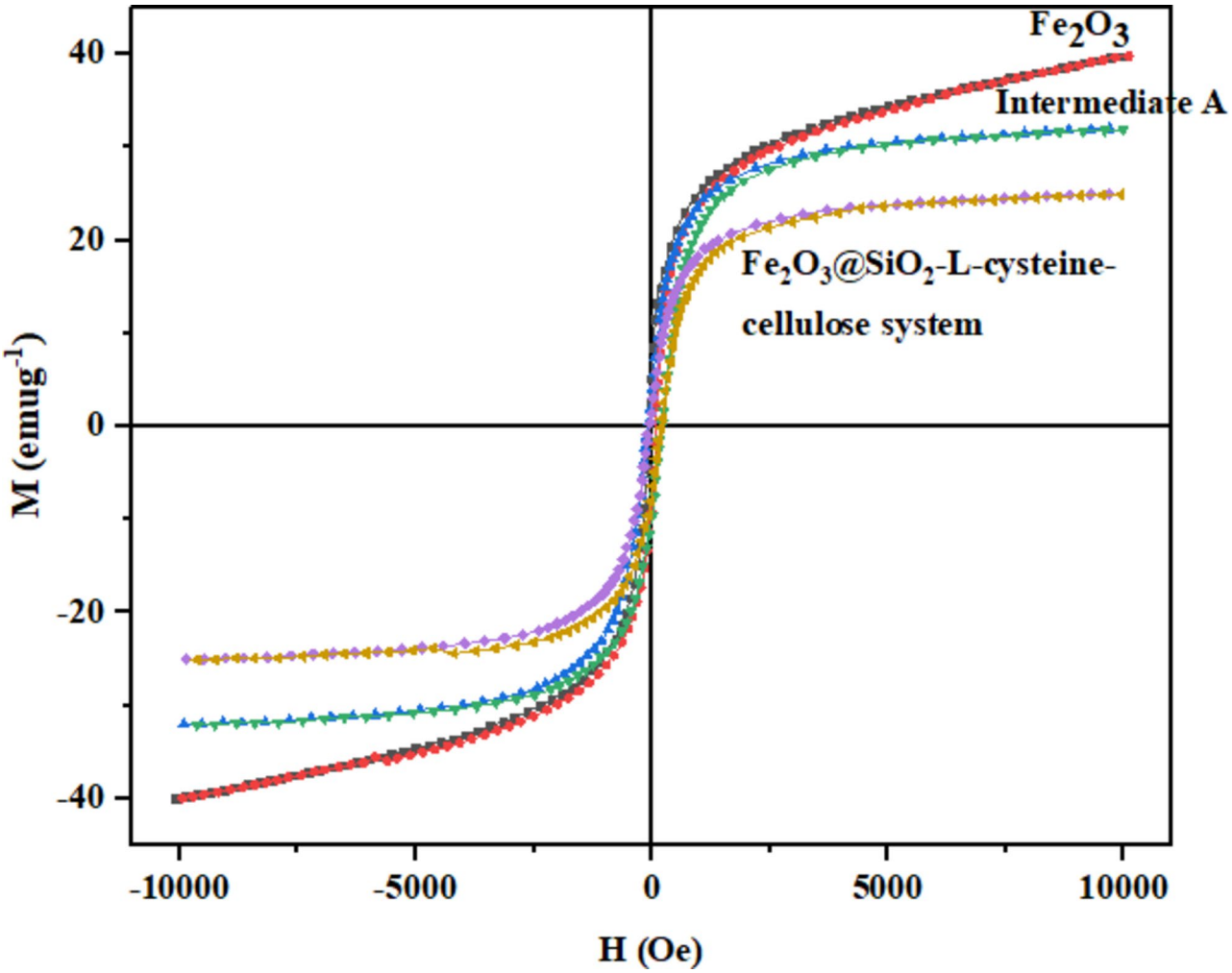

Fig. 6. VSM analysis of Fe_2O_3, intermediate **A**, and Fe_2O_3@SiO_2-L-cysteine-cellulose system.

Sample	M_s (memu/g)	M_r (memu/g)	H_c (Oe)
Fe_2O_3	39.67	6.47	−110.23
Intermediate A	32.00	4.204	−227.09
Fe_2O_3@SiO_2-L-cysteine-cellulose system	24.88	2.274	−229.53

Table 1. Magnetic parameters of Fe2O3, intermediate A, and Fe2O3@SiO2-L-cysteine-cellulose system.

Sample	FS (MPa)	FM (GPa)	CS (GPa)
Intermediate A	39.64	1.42	61.25
TiO_2@SiO_2-alkyl-NH_2 grafted cellulose	86.96	4.12	106.58

Table 2. Mechanical characteristics of Fe2O3@SiO2-L-cysteine-cellulose system.

The process of mass-increasing was used for the calculation of the CO_2 adsorption capacity of the Fe_2O_3@SiO_2-L-cysteine-cellulose system and the results are depicted in Fig. 9. The presence of COOH, NH, and OH functional groups increased the potential of the adsorbent for the adsorption of CO_2 gas. The progress of the CO_2 adsorption-desorption studies was done in three steps. At first, the sample was degassed by the N_2 at 150 °C, and then the sample was cooled to 40 °C followed by N_2 flow for 30 min. Next, the CO_2 adsorption was done using a mixture of CO_2/N_2 (30% CO_2) with a flow of 60 mL/min. The final step is the desorption of CO_2 using a flow of N_2 from the surface of the Fe_2O_3@SiO_2-L-cysteine-cellulose system. During the final step, the temperature decreased to 10 °C, and CO_2 was desorbed from the sample surface. As revealed, the Fe_2O_3@SiO_2-L-cysteine-

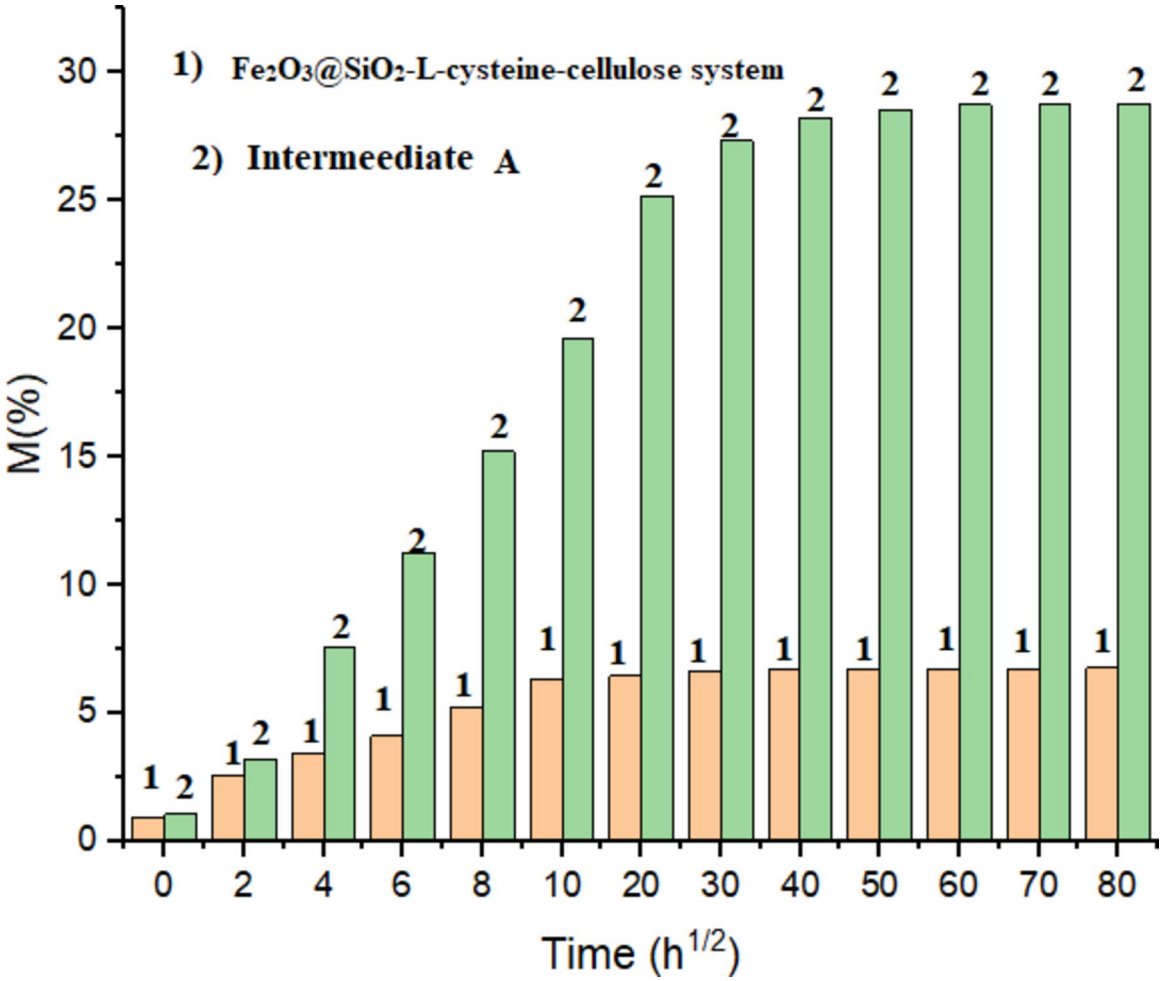

Fig. 7. Water adsorption of intermediate **A**, and Fe_2O_3@SiO_2-L-cysteine-cellulose system.

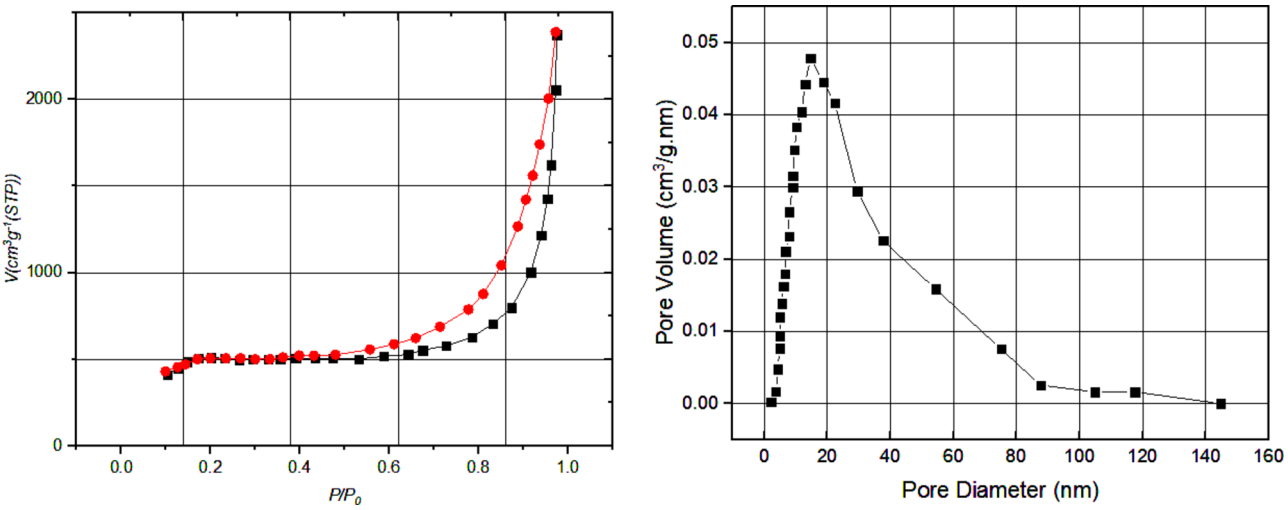

Fig. 8. N_2 adsorption-desorption capacity (inside, pore volume, and pore diameter) of Fe_2O_3@SiO_2-L-cysteine-cellulose system.

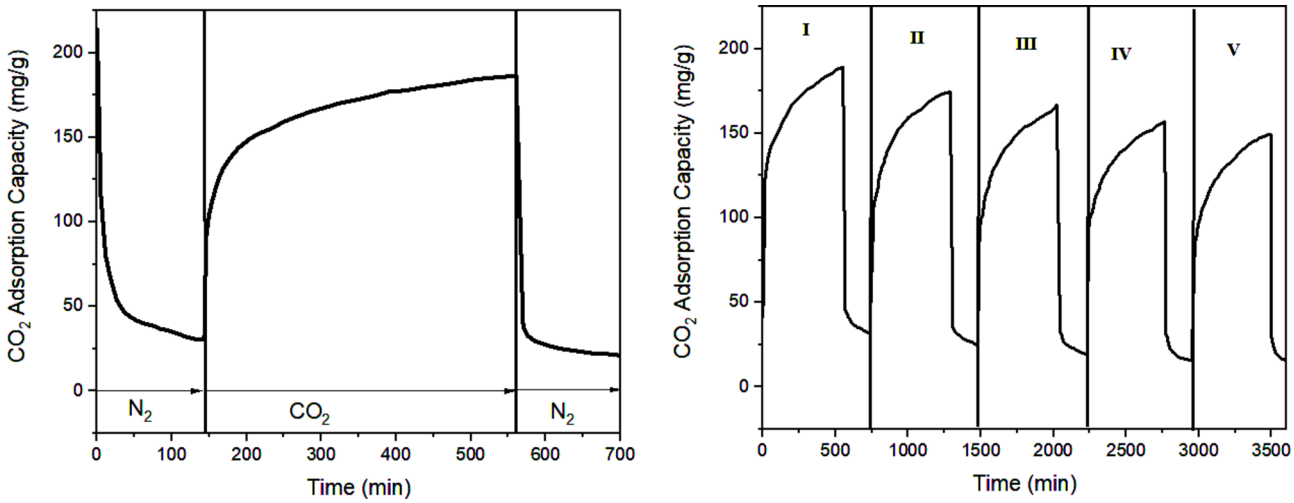

Fig. 9. CO_2 adsorption-desorption capacity (inside, recycling test) of Fe_2O_3@SiO_2-L-cysteine-cellulose system.

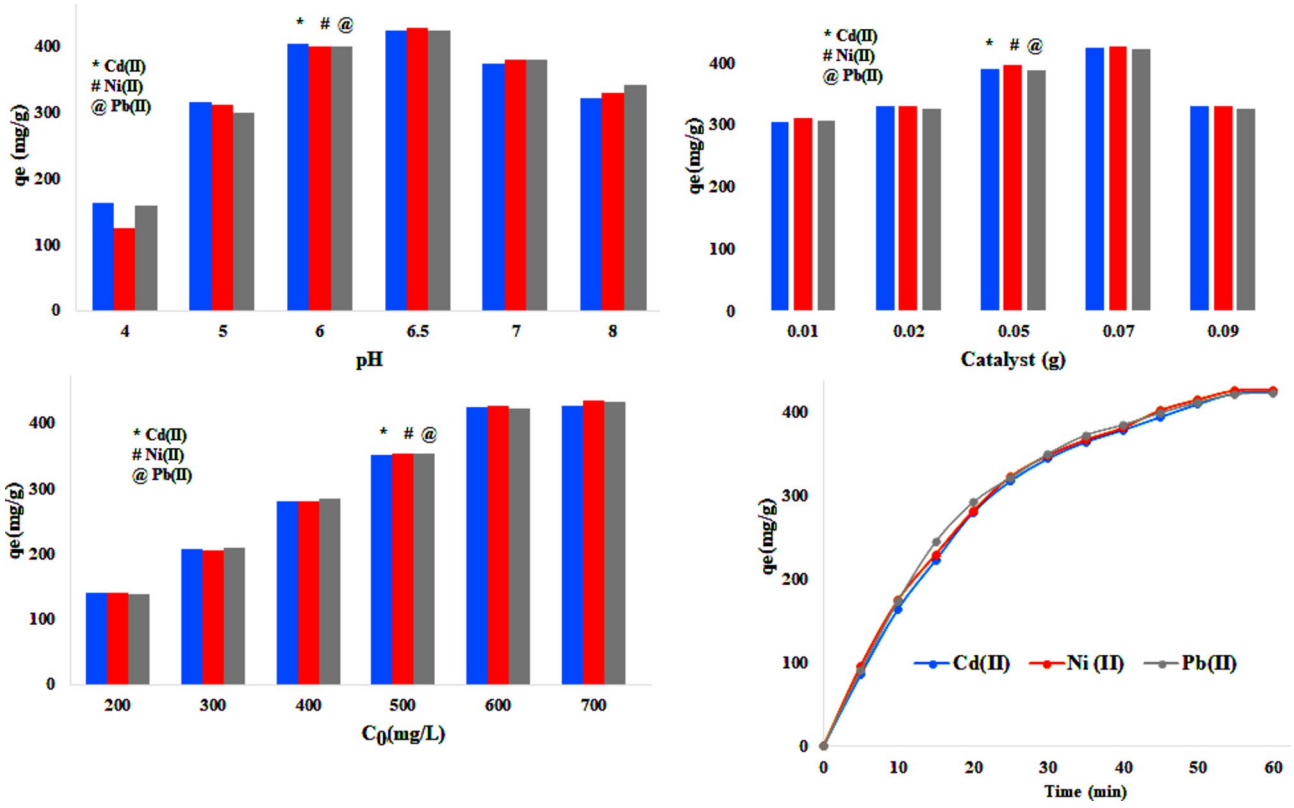

Fig. 10. Adsorption of Pb(II), Ni(II), and Cd(II) ions.

cellulose system has a high potential for CO_2 adsorption and their adsorption capacity was reached up to 180 mg CO_2 per gram of adsorbent.

The adsorption-desorption of CO_2 was also investigated in five cycles at 40 °C (Fig. 9). As revealed, the recycling potential of Fe_2O_3@SiO_2-L-cysteine-cellulose system is good and the sample is stable during the process.

Adsorption studies for cd(II)/Ni(II)/Pb(II) ions

The effectiveness of the Fe_2O_3@SiO_2-L-cysteine-cellulose composite as an adsorbent was further explored. The adsorption performance for removing Cd(II), Ni(II), and Pb(II) ions from wastewater is presented in Fig. 10. A range of variables was analyzed, including pH (4 to 8), metal ion concentration (200–700 mg/L), adsorption

duration (0–60 min), and catalyst dosage (0.01 g to 0.09 g) to identify the optimal conditions for maximum adsorption capacity.

All experiments were conducted at room temperature (298 K) with a solution volume of 50 mL. The results demonstrate that the adsorption capacity increases significantly within the first 40 min, gradually approaching equilibrium thereafter. The highest adsorption capacity (qe) was achieved at a pH of 6.5, a catalyst dosage of 0.07 g, and a metal ion concentration of 500 mg/L. It was observed that in highly acidic conditions (pH < 6), H^+ ions compete with metal ions for interaction with the functional groups (COOH, NH, and OH) on the Fe_2O_3@SiO_2-L-cysteine-cellulose composite. On the other hand, as the pH rises and becomes more basic, OH^- ions predominate, leading to the precipitation of metal ions as metal hydroxides, which inhibits adsorption (see Fig. 10).

Increasing the dosage of the adsorbent from 0.01 g to 0.07 g significantly enhanced the adsorption capacity, as shown in Fig. 10. This improvement is due to the higher availability of active sites on the adsorbent, facilitating more effective capture of contaminants. However, when the dosage was further increased to 0.09 g, a decline in adsorption capacity was noted. This decrease can be explained by the incomplete saturation of adsorption sites and the agglomeration of adsorbent particles at higher dosages, which reduces the effective surface area available for adsorption. Additionally, particle clustering can adversely affect overall adsorption performance. Figure 10 illustrates that the adsorption capacity also rises substantially with higher initial concentrations of Cd(II), Ni(II), and Pb(II) ions, peaking at a concentration of 600 mg/L. This trend can be understood by the increased mass transfer driving force, which enhances the interaction between the metal ions and the adsorbent. Beyond this concentration, the adsorption capacity levels off, indicating that the adsorbent has reached its saturation limit. At this point, all active sites on the adsorbent are filled, preventing any additional ions in the solution from being adsorbed, which results in a plateau in adsorption capacity despite further increases in ion concentration.

The FT-IR analysis of the adsorbent before and after the adsorption of Pb(II) ions simply confirms this decision. The FT-IR spectra of the Fe_2O_3@SiO_2-L-cysteine-cellulose system before and after Pb(II) adsorption reveal significant structural changes, highlighting the functional groups involved in the adsorption process (Fig. 11). The broadband in the 3100–3600 cm^{-1} region, attributed to O-H stretching vibrations, shifts to lower

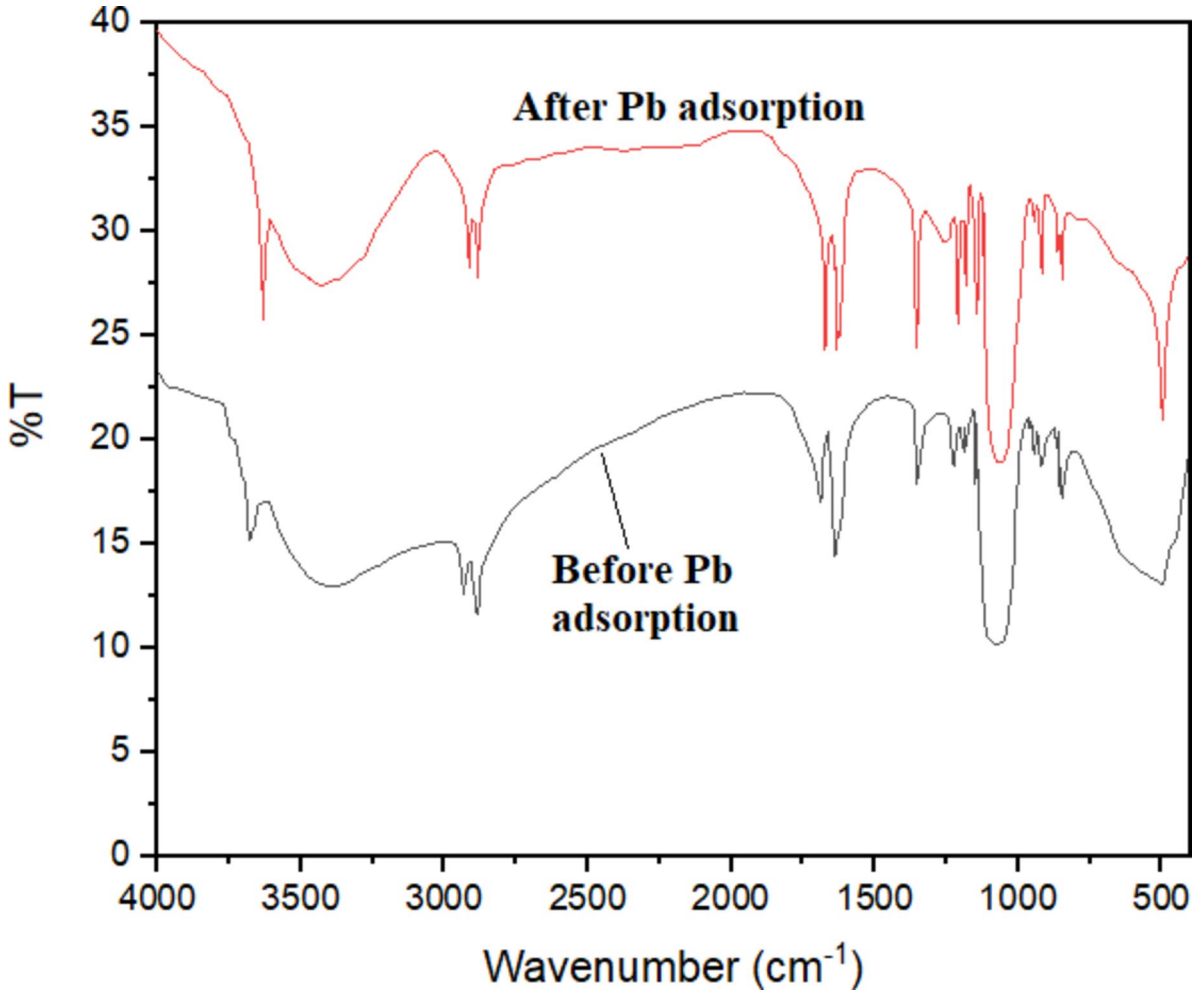

Fig. 11. FT-IR analysis of Fe_2O_3@SiO_2-L-cysteine-cellulose system before (below) and after (up) adsorption of Pb(II) ions.

wavenumbers, and broadband decreases in intensity after adsorption, indicating the participation of hydroxyl groups in binding Pb(II) ions. The band related to the N-H group at above 3600 cm^{-1} shows similar behavior. Similarly, the carbonyl (C = O) stretching vibrations around 1650–1750 cm^{-1} show a shift and reduction in intensity, suggesting their involvement in complexation. Conversely, the characteristic Si–O–Si and Fe-O vibrations (400–1200 cm^{-1}) remain stable, confirming the structural integrity of the Fe_2O_3@SiO_2 framework during adsorption. These observations underscore the critical role of hydroxyl, amine, carbonyl, and carboxyl groups in Pb(II) binding, while the robust framework of the adsorbent ensures its structural stability and effectiveness in heavy metal removal.

Adsorption studies for cr(VI) ions

Hexavalent chromium (Cr(VI)), typically present as $HCrO_4^-$, CrO_4^{2-}, and $Cr_2O_7^{2-}$, is widely used in industries like metallurgy, tanning, and electroplating. These industrial activities produce vast amounts of wastewater laden with Cr(VI), which poses a dire threat to human health due to its extreme toxicity and its carcinogenic, teratogenic, and mutagenic effects. Cr(VI) can penetrate the human body through the food chain, exacerbating its hazardous impact. Therefore, it is imperative to employ a wastewater treatment method that delivers high removal efficiency, is cost-effective, and is straightforward to operate, to mitigate this serious environmental and public health issue[48–51].

Our study focused on identifying the optimal pH for the reaction medium, given that Cr(VI) species adopt different forms depending on the pH: H_2CrO_4 in strongly acidic conditions, $HCrO_4^-$ in moderately acidic conditions, and $Cr_2O_7^{2-}$ in neutral to basic conditions. Consequently, the pH of the reaction medium is a critical factor influencing the adsorption capacity of the Fe_2O_3@SiO_2-L-cysteine-cellulose system[48–51].

To identify the optimal pH for Cr(VI) removal, we investigated the effect of pH on the adsorption process using the Fe_2O_3@SiO_2-L-cysteine-cellulose composite over a range of 2 to 8. The results, presented in Fig. 12, reveal that the adsorption of Cr(VI) decreases significantly as pH increases. At pH values below 5, the surface of the composite is positively charged, while it becomes negatively charged at pH values above 5. In acidic conditions, Cr(VI) mainly exists as negatively charged anions ($HCrO_4^-$ and $HCr_2O_7^-$). The strong electrostatic interactions between these negatively charged species and the positively charged sites on the composite enhance adsorption in acidic environments, as depicted in Fig. 12. The peak adsorption capacity (q_e) was recorded at pH 4, with a catalyst dosage of 0.07 g and a metal ion concentration of 90 mg/L. The findings suggest that at lower pH values (pH < 4), there is competition between H^+ ions and Cr(VI) species (H_2CrO_4 and $H_2Cr_2O_7$) for binding to the COOH, protonated NH, and OH groups on the composite. Conversely, at pH levels above 6, all Cr(VI) species are negatively charged (CrO_4^{2-} and $Cr_2O_7^{2-}$) and do not interact with the negatively charged carboxylate groups present on the adsorbent, as illustrated in Fig. 12.

The investigation focused on the effects of metal ion concentration (20–100 mg/L) and catalyst dosage (0.01 g to 0.09 g) to establish the optimal conditions for maximum adsorption. All tests were carried out at

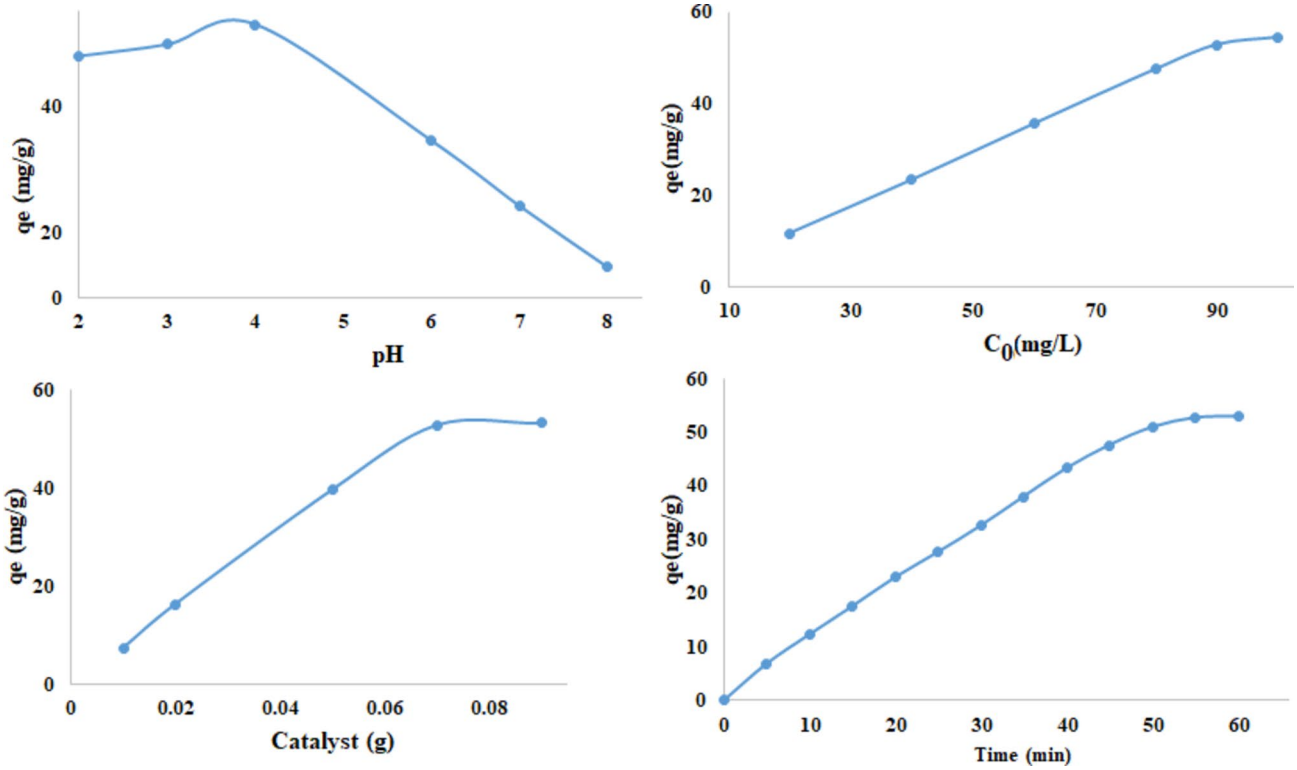

Fig. 12. Adsorption of Cr(VI) ions.

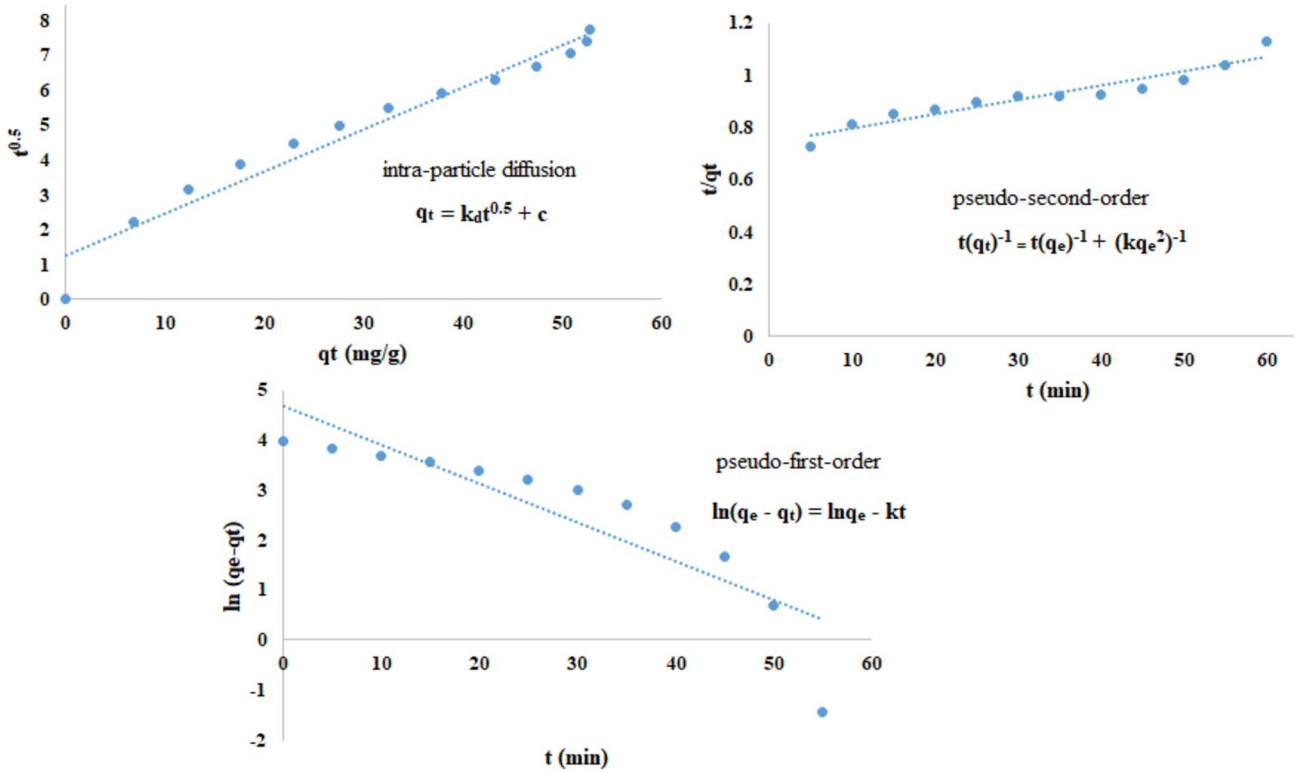

Fig. 13. Kinetic models and equations for the adsorption of Cr(VI).

Kinetic models	Parameters
Pseudo-first-order	k = 0.0774 (R^2 = 0.7765) q_e = 107.32 mg/g
Pseudo-second-order	k = 4.08*10^{-5} (R^2 = 0.9066) q_e = 181.81 mg/g
Intra-particle diffusion	k_d = 0.1211 (R^2 = 0.9552) c = 1.2556

Table 3. Parameters and correlation coefficient (R2) of kinetic models.

ambient temperature (298 K) with a solution volume of 50 mL. The results indicated that the best conditions for adsorption were achieved with 0.07 g of the adsorbent, resulting in an adsorption efficiency exceeding 98% at an initial Cr(VI) concentration of 90 mg/L (Fig. 12). In contrast, increasing the initial Cr(VI) concentration to 500 mg/L led to a significant drop in adsorption efficiency to below 40%. The study also rigorously assessed the impact of contact time on the uptake of Cr(VI), as illustrated in Fig. 12. The findings demonstrate that the removal percentage of Cr(VI) from the solution increased significantly with longer contact times, peaking before gradually leveling off to reach equilibrium at 60 min. The initial rapid removal rate can be attributed to the high availability of sorption sites on the adsorbent at the beginning of the adsorption process.

To thoroughly understand the adsorption behavior of Cr(VI) on the synthesized samples, a detailed analysis was performed using multiple kinetic models, including the pseudo-first-order, pseudo-second-order, and intra-particle diffusion models. Figure 13 presents the equations and plots related to these models. The plots of $\ln(q_e - q_t)$ versus time for the pseudo-first-order model, qt versus $t^{0.5}$ for intra-particle diffusion, and t/q_t versus time for the pseudo-second-order model are displayed in Fig. 13. These graphs enabled the calculation of rate constants and the estimated equilibrium adsorption capacity. The kinetic parameters and calculated adsorption capacities are summarized in Table 3. The results clearly showed that the intra-particle diffusion model exhibited the best fit with the experimental data, indicated by a high correlation coefficient (R^2 = 0.9552), confirming that intra-particle diffusion is the dominant process controlling Cr(VI) adsorption in this system.

To gain a better understanding of the adsorption of Cr(VI) onto the Fe_2O_3@SiO_2-L-cysteine-cellulose adsorbent system, four isotherm models (Langmuir, Freundlich, Temkin, and Dubinin-Radushkevich) were evaluated and graphed (Fig. 14). The analysis revealed that the Freundlich isotherm yielded the best fit with an R^2 value of 0.992, suggesting a heterogeneous surface with multiple adsorption sites that have different affinities for Cr(VI). As the concentration of Cr(VI) increases, the adsorption rate decreases, indicating that not all available sites are equally effective in binding the contaminant. The Temkin and Dubinin-Radushkevich models also demonstrated reasonable fits, with R^2 values of 0.967 and 0.913, respectively, indicating that the adsorption process involves significant interactions between the adsorbent and Cr(VI) at lower concentrations, with a

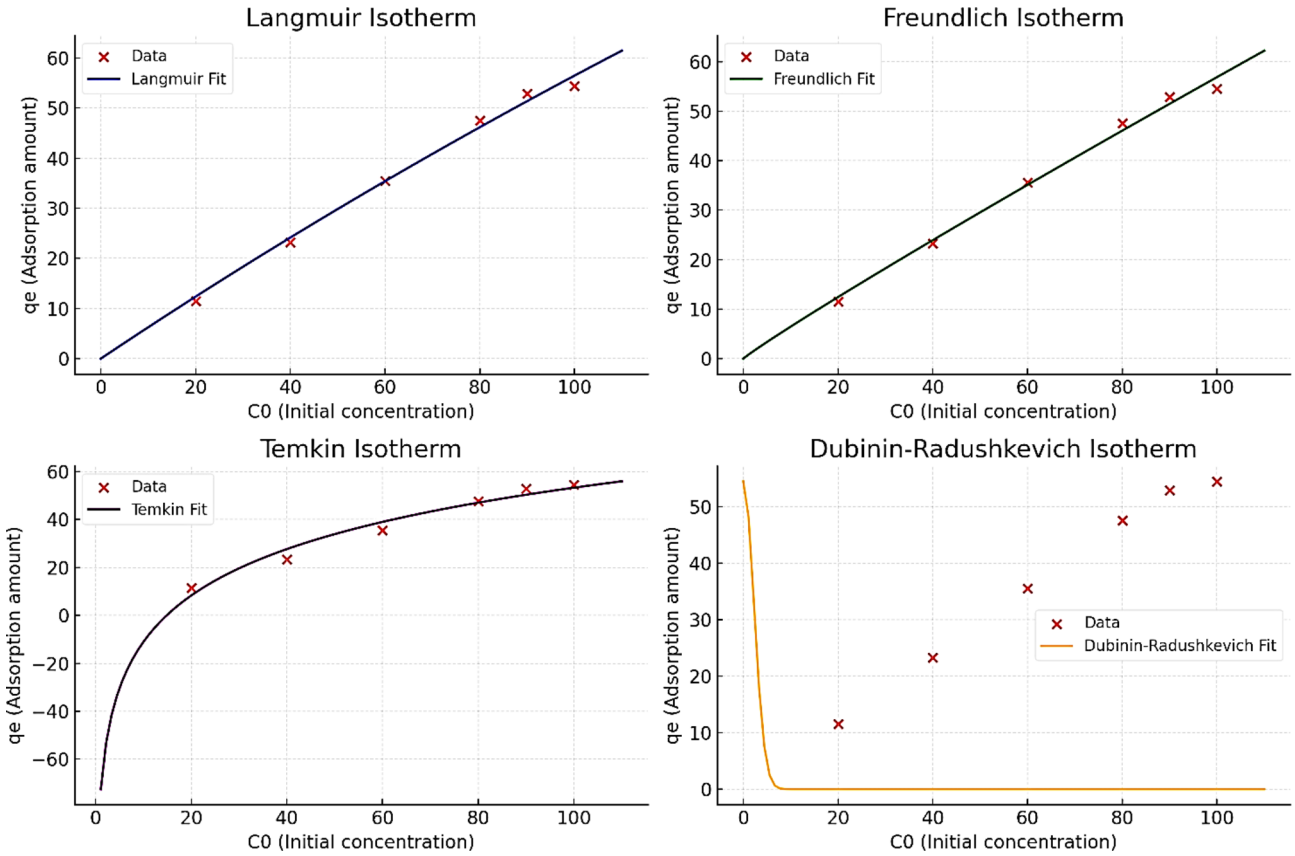

Fig. 14. Isotherm models calculated for the adsorption of Cr(VI) [Calculated parameters for Langmuir Isotherm (Q_{max}: 37.55 mg/g; K_L: −5539230.42; R^2: −0.000000011), Freundlich Isotherm (K_F: 0.733; n: 1.059; R^2: 0.992), Temkin Isotherm (B: 27.94; K_T: 0.0672; R^2: 0.967), Dubinin-Radushkevich Isotherm (Q_{max}: 61.61 mg/g; β: 1582.26; R^2: 0.913)]

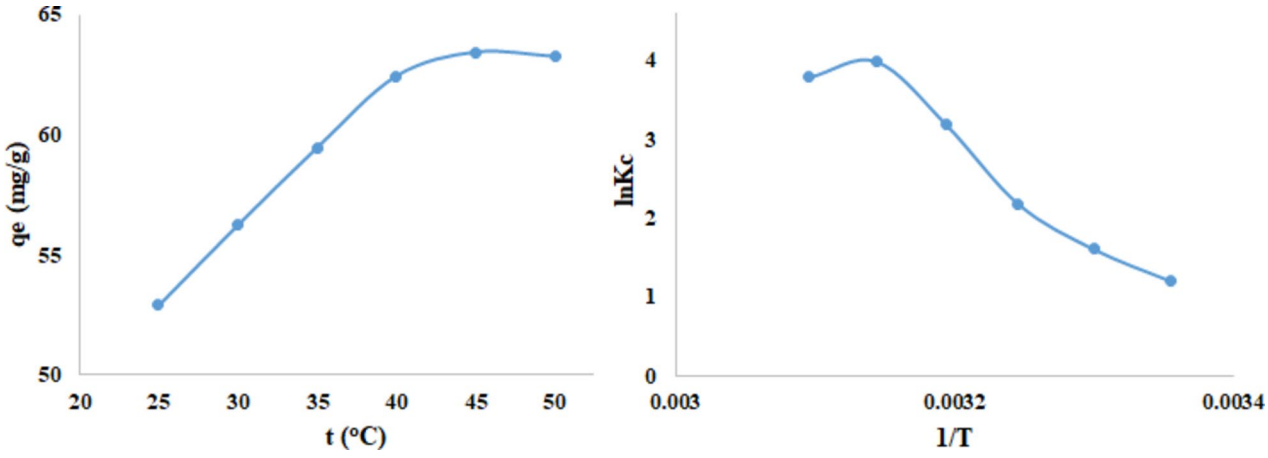

Fig. 15. Adsorption studies of Cr(VI): effect of temperature (left), plot of lnKc versus 1/T (right).

distribution of energy across the adsorption sites. The Langmuir model, however, did not fit well, suggesting that a monolayer adsorption process on a homogeneous surface does not adequately describe the behavior of Cr(VI) on this adsorbent system. These findings indicate that the adsorption of Cr(VI) is primarily governed by surface characteristics and interaction energies, revealing that the system favors a combination of physical and chemical adsorption mechanisms with varying levels of interaction at different concentrations[52].

Figure 15 clearly shows that higher temperatures significantly enhance both the adsorption capacity and removal rate of Cr(VI). As the temperature increases, the total adsorption time extends, and the adsorption

ΔG° (Kj/mol)	ΔS° (j/mol)	ΔH° (Kj/mol)
−2.97 (T = 298 K), -−.58 (T = 308 K), -−.40 (T = 318 K), -−.69 (T = 328 K), -−1.21 (T = 338 K), −10.12 (T = 348 K)	332.56	96.56

Table 4. Thermodynamic parameters for the adsorption of cr(VI).

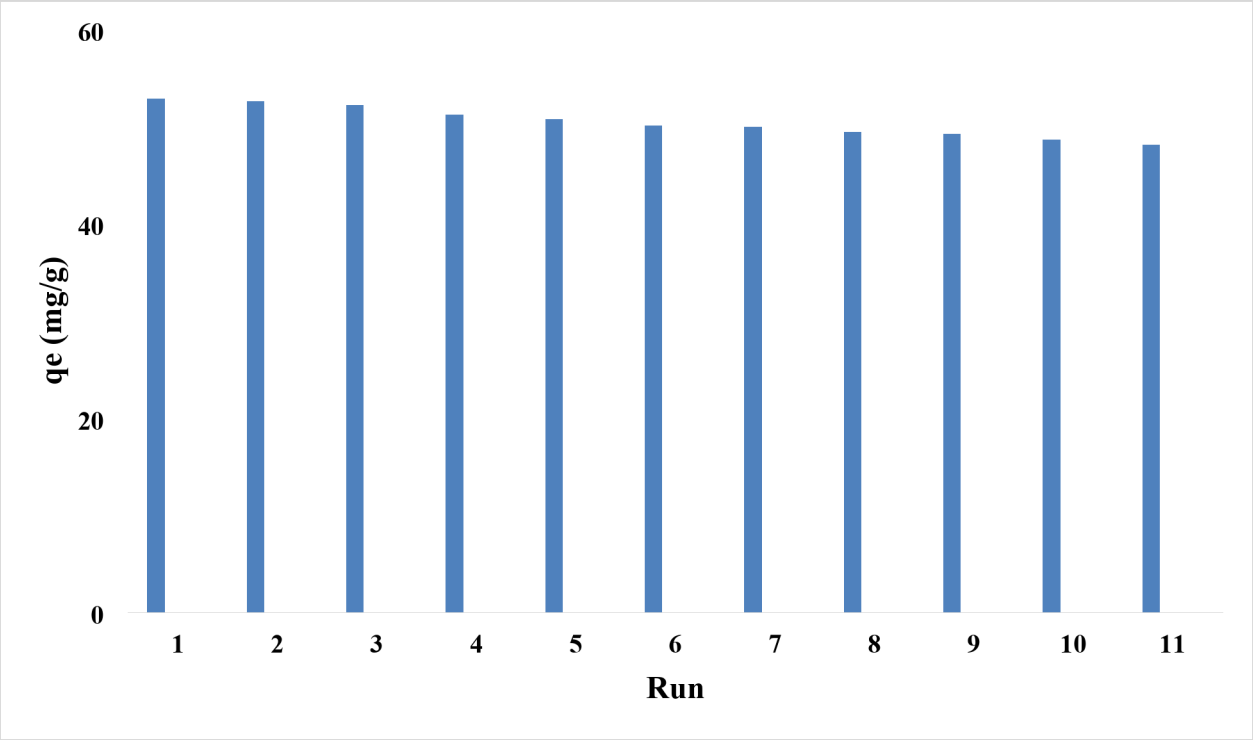

Fig. 16. Recovery and reusability of Fe_2O_3@SiO_2-L-cysteine-cellulose system.

capacity of S6 rises dramatically, reaching 63.45 mg/g at 65 °C. This indicates that the adsorption process for Cr(VI) is endothermic, meaning it absorbs heat, with higher temperatures leading to greater adsorption capacity. A detailed thermodynamic analysis was conducted to gain insights into the process.

The Gibbs free energy (ΔG), enthalpy (ΔH), and entropy (ΔS) of the system were calculated to understand the feasibility, heat exchange, and disorder changes during adsorption. ΔG values for Cr(VI) ions at six different temperatures were determined using the relationship between ΔG, ΔH, ΔS, and the equilibrium constant (Kc), as outlined in Table 4. The ΔH and ΔS values were derived from the plot of LnKc against 1/T, as depicted in Fig. 15. The values of ΔG, ΔH, and ΔS detailed in Table 4 provide profound insights into the adsorption of Cr(VI).

This plot, known as the Van't Hoff plot, provided a linear relationship from which ΔH and ΔS were derived. The positive ΔH value confirmed the endothermic nature of the adsorption, indicating that heat is absorbed during the process. The positive ΔS value suggested an increase in disorder at the solid-liquid interface. The values of ΔG, ΔH, and ΔS listed in Table 4 offer a comprehensive understanding of Cr(VI) adsorption. The negative ΔG values at elevated temperatures suggest that the adsorption process is spontaneous and thermodynamically favorable under these conditions. This thorough thermodynamic analysis highlights the significant role of temperature in enhancing the adsorption capacity and efficiency for Cr(VI) removal, providing valuable information for optimizing the process in practical applications.

The following formulas were utilized for the calculations:$\Delta G^\circ = -RTInK_c$ $K_c = \frac{q_e}{C_e}$ $RTInK_c = T\Delta S^\circ - \Delta H^\circ$

Kc (L/mg) is the equilibrium constant, R = 8.314 J/molK, T is the absolute temperature (K).

Physisorption is typically regarded as irreversible due to the weak interactions between the adsorbate molecules and the adsorbent surface. It was found that increasing the solution pH is highly effective for regenerating the Fe_2O_3@SiO_2-L-cysteine-cellulose system. The desorption experiments were done using NaOH solution (0.1 M). After regeneration, the pH was adjusted to 7 with distilled water, and recycling experiments confirmed that Fe_2O_3@SiO_2-L-cysteine-cellulose system can be reused up to 11 times, with good adsorption efficiencies (Fig. 16). The progressive decrease in adsorption efficiency with each cycle is due to the partial blockage of active sites, which cannot be fully desorbed by the regenerating.

The synthesized catalyst demonstrated an adsorption capacity of 52.89 mg/g for Cr(VI), measured under optimized conditions (pH 4, a catalyst dosage of 0.07 g, and a metal ion concentration of 90 mg/L). This performance is comparable to, although slightly lower than, several other adsorbents reported in the literature.

Adsorbent	Adsorption capacity (qe) (mg/g)	Conditions	Reference
Synthesized catalyst (this work)	52.89	pH 4, 0.07 g dosage, 90 mg/L	–
Chitosan-coated Fe_3O_4	35.7	pH 5, 0.1 g dosage, 50 mg/L	[53]
Activated carbon from rice husk	45.2	pH 3, 0.05 g dosage, 100 mg/L	[54]
Magnetic graphene oxide	72.3	pH 4, 0.02 g dosage, 50 mg/L	[55]
Zeolite coated with ionic liquid	50.5	pH 4, 0.08 g dosage, 80 mg/L	[56]
Biochar from pinewood	40.6	pH 6, 0.1 g dosage, 75 mg/L	[57]
Mn-doped Fe_3O_4 nanoparticles	60.4	pH 3, 0.05 g dosage, 80 mg/L	[58]
Amino-functionalized silica	48.8	pH 5, 0.1 g dosage, 100 mg/L	[59]
Hydrothermally modified biochar	58.2	pH 3, 0.05 g dosage, 90 mg/L	[60]
Polyaniline nanocomposite	65.5	pH 2, 0.04 g dosage, 100 mg/L	[61]
Fe-Al layered double hydroxide	54.3	pH 4, 0.06 g dosage, 75 mg/L	[62]
Carbonized tea waste	41.7	pH 5, 0.1 g dosage, 50 mg/L	[63]
Magnetized corn straw	49.6	pH 3, 0.08 g dosage, 90 mg/L	[64]

Table 5. Comparison results of cr(VI) adsorption capacities.

For instance, magnetic graphene oxide and Mn-doped Fe_3O_4 nanoparticles exhibited higher adsorption capacities of 72.3 mg/g and 60.4 mg/g, respectively. In contrast, other materials, such as biochar from pinewood and hydrothermally modified biochar, showed capacities of 40.6 mg/g and 58.2 mg/g, respectively, placing them in a similar range to the synthesized catalyst. These findings highlight the effectiveness of the synthesized catalyst in removing Cr(VI) from aqueous solutions, with performance on par with more complex adsorbents. Despite its slightly lower adsorption capacity than some high-performance materials, the synthesized catalyst offers significant advantages, such as ease of synthesis, cost-effectiveness, and sustainability, making it an attractive option for large-scale applications. Additionally, the material's potential for regeneration could provide long-term economic and environmental benefits. These results emphasize the importance of considering adsorption capacity and the practical aspects of catalyst preparation, cost, and reusability when selecting materials for ecological applications (Table 5).

Conclusion

In this investigation, a Fe_2O_3@SiO_2-L-cysteine-cellulose composite adsorbent was developed through a straightforward synthesis process and characterized using techniques such as XRD, EDS, FT-IR, and TGA-DTA. The performance of the adsorbent in removing heavy metal ions, including Cr(VI), Cd(II), Ni(II), and Pb(II), from wastewater was assessed. Various factors influencing the adsorption process, including pH, adsorbent dosage, metal ion concentration, and temperature, were systematically studied. Optimal conditions for adsorption were identified at a pH of 6.5, a metal ion concentration of 600 mg/L, and an adsorbent dosage of 0.07 g, all at room temperature, leading to the most effective removal of heavy metals. Furthermore, the Fe_2O_3@SiO_2-L-cysteine-cellulose system also demonstrated significant potential for the adsorption of N_2 and CO_2 gases, underscoring its applicability in both liquid and gaseous environments.

Data availability

The datasets used and/or analysed during the current study available from the corresponding author on reasonable request.

Received: 10 November 2024; Accepted: 10 February 2025
Published online: 11 March 2025

References

1. Stern, R. & Jedrzejas, M. J. Carbohydrate polymers at the center of life's origins: the importance of molecular processivity. *Chem. Rev.* **108**, 5061–5085. https://doi.org/10.1021/cr078240l (2008).
2. Di, X. et al. Carbohydrates used in polymeric systems for drug delivery: from structures to applications. *Pharmaceutics* **14**, 739. https://doi.org/10.3390/pharmaceutics14040739 (2022).
3. Rashid, A. B. et al. Synthesis, properties, applications, and future prospective of cellulose nanocrystals. *Polymers* **15**, 4070. https://doi.org/10.3390/polym15204070 (2023).
4. Zaman, A., Huang, F., Jiang, M., Wei, W. & Zhou, Z. Preparation, properties, and applications of natural cellulosic aerogels: a review. *Energy Built Environ.* **1**, 60–76. https://doi.org/10.1016/j.enbenv.2019.09.002 (2020).
5. Kayra, N. & Aytekin, A. Ö. Synthesis of cellulose-based hydrogels: Preparation, formation, mixture, and modification. In *Cellulose-Based Superabsorbent Hydrogels*. (ed Mondal, M.) https://doi.org/10.1007/978-3-319-77830-3_16. (Springer, Cham, 2019).
6. Torkian, P., Mortazavi Najafabadi, S. M., Grzelczyk, D. & Ghashang, M. TiO_2 bonded SiO_2-alkyl-NH_2 grafted cellulose for improving thermal stability, mechanical strength characteristics, and water adsorption capacity. *Cellulose* **31** (3), 1801–1812. https://doi.org/10.1007/s10570-024-05123-x (2024).
7. Gupta, A. D., Kirti, N., Katiyar, P. & Singh, H. A critical review on three-dimensional cellulose-based aerogels: synthesis, physico-chemical characterizations and applications as adsorbents for heavy metals removal from water. *Cellulose* **30**, 3397–3427. https://doi.org/10.1007/s10570-023-05129-4 (2023).
8. Li, X. et al. An overview of the development status and applications of cellulose-based functional materials. *Cellulose* **31**, 61–99. https://doi.org/10.1007/s10570-023-05616-8 (2024).

9. Azimi, B. et al. Application of cellulose-based materials as water purification filters; a state-of-the-art review. *J. Polym. Environ.* **32**, 345–366. https://doi.org/10.1007/s10924-023-02989-6 (2024).
10. Hu, Z. et al. Amine-functionalized cellulose nanofiber-sodium alginate-Fe(III) porous hollow beads for the efficient removal of cr(VI). *Cellulose* **30**, 3807–3822. https://doi.org/10.1007/s10570-023-05123-w (2023).
11. Kumar, A. & Kumar, V. A comprehensive review on application of lignocellulose derived nanomaterial in heavy metals removal from wastewater. *Chem. Afr.* **6**, 39–78. https://doi.org/10.1007/s42250-022-00367-8 (2023).
12. Si, R., Pu, J., Luo, H., Wu, C. & Duan, G. Nanocellulose-based adsorbents for heavy metal ion. *Polymers* **14**, 5479. https://doi.org/10.3390/polym14245479 (2022).
13. Razzak, S. A. et al. M. A comprehensive review on conventional and biological-driven heavy metals removal from industrial wastewater. *Environ. Adv.* **7**, 100168. https://doi.org/10.1016/j.envadv.2022.100168 (2022).
14. Abd Elnabi, M. K. et al. Toxicity of heavy metals and recent advances in their removal: a review. *Toxics* **11**, 580. https://doi.org/10.3390/toxics11070580 (2023).
15. Pandey, A., Kalamdhad, A. & Sharma, Y. C. Recent advances of nanocellulose as biobased adsorbent for heavy metal ions removal: a sustainable approach integrating with waste management. *Environ. Nanotechnol. Monit. Manag.* **20**, 100791. https://doi.org/10.1016/j.enmm.2023.100791 (2023).
16. Munshi, A. M. et al. Thiophene functionalized cellulose immobilized with metal organic framework for removal of heavy metals. *Cellulose* **30**, 7235–7250. https://doi.org/10.1007/s10570-023-05331-4 (2023).
17. Iqbal, S. H., Muthukumaran, S. & Baskaran, K. Polyglutamic acid and its derivatives as multi-functional biopolymers for the removal of heavy metals from water: a review. *J. Water Process. Eng.* **56**, 104367. https://doi.org/10.1016/j.jwpe.2023.104367 (2023).
18. Ugwu, D. I. & Conradie, J. The use of bidentate ligands for heavy metal removal from contaminated water. *Environ. Adv.* **15**, 100460. https://doi.org/10.1016/j.envadv.2023.100460 (2024).
19. Jiang, J. et al. Utilizing adsorption of wood and its derivatives as an emerging strategy for the treatment of heavy metal-contaminated wastewater. *Environ. Pollut.* **340**, 122830. https://doi.org/10.1016/j.envpol.2023.122830 (2024).
20. Jadoun, S., Fuentes, J. P., Urbano, B. F. & Yáñez, J. A review on adsorption of heavy metals from wastewater using conducting polymer-based materials. *J. Environ. Chem. Eng.* **11**, 109226. https://doi.org/10.1016/j.jece.2022.109226 (2023).
21. Velarde, L., Nabavi, M. S., Escalera, E., Antti, M. L. & Akhtar, F. Adsorption of heavy metals on natural zeolites: a review. *Chemosphere* **328**, 138508. https://doi.org/10.1016/j.chemosphere.2023.138508 (2023).
22. Aminsharei, F., Lahijanian, A., Shiehbeigi, A., Beiki, S. S. & Ghashang, M. Dual magnetization and amination of cellulosic chains for the efficient adsorption of heavy metals. *Int. J. Biol. Macromol.* **276**, 134004. https://doi.org/10.1016/j.ijbiomac.2024.134004 (2024).
23. Doyo, A. N., Kumar, R. & Barakat, M. A. Recent advances in cellulose, chitosan, and alginate-based biopolymeric composites for adsorption of heavy metals from wastewater. *J. Taiwan Inst. Chem. Eng.* **151**, 105095. https://doi.org/10.1016/j.jtice.2023.105095 (2023).
24. Ren, H. et al. Facile synthesis of nitrogen, sulfur co-doped carbon quantum dots for selective detection of mercury (II). *Environ. Chem. Lett.* **22**, 35–41. https://doi.org/10.1007/s10311-023-01660-9 (2024).
25. Labidi, A. et al. Coal ash for removing toxic metals and phenolic contaminants from wastewater: a brief review. *Environ. Sci. Pollut. Res.* **30**, 2006–2029. https://doi.org/10.1080/10643389.2023.2206781 (2023).
26. Labidi, A., Salaberria, A. M., Fernandes, S. C. M., Labidi, J. & Abderrabba, M. Microwave-assisted synthesis of poly (N-vinylimidazole) grafted chitosan as an effective adsorbent for mercury (II) removal from aqueous solution: equilibrium, kinetic, thermodynamics and regeneration studies. *J. Polym. Environ.* **27**, 828–840. https://doi.org/10.1080/01932691.2019.1614025 (2019).
27. Labidi, A., Salaberria, A. M., Labidi, J. & Abderrabba, M. Preparation of novel carboxymethylchitosan-graft-poly(methylmethacrylate) under microwave irradiation as a chitosan-based material for Hg^{2+} removal. *Microchem. J.* **148**, 531–540. https://doi.org/10.1016/j.microc.2019.05.029 (2019).
28. Labidi, A., Salaberria, A. M., Fernandes, S. C. M., Labidi, J. & Abderrabba, M. Adsorption of copper on chitin-based materials: kinetic and thermodynamic studies. *J. Taiwan Inst. Chem. Eng.* **65**, 140–148. https://doi.org/10.1016/j.jtice.2016.04.030 (2016).
29. Ren, H. et al. Turning agroforestry waste into value-added fluorescent carbon quantum dots for effective detection of Fe^{3+} in an aqueous environment. *ACS EST Eng.* **3**, 260–270. https://doi.org/10.1021/acsestengg.2c00294 (2023).
30. Liu, L. et al. Fabrication of novel magnetic core-shell chelating adsorbent for rapid and highly efficient adsorption of heavy metal ions from aqueous solution. *J. Mol. Liq.* **313**, 113593. https://doi.org/10.1016/j.molliq.2020.113593 (2020).
31. Ren, Y., Abbood, H. A., He, F., Peng, H. & Huang, K. Magnetic EDTA-modified chitosan/SiO_2/Fe_3O_4 adsorbent: Preparation, characterization, and application in heavy metal adsorption. *Chem. Eng. J.* **226**, 300–311. https://doi.org/10.1016/j.cej.2013.04.059 (2013).
32. Xu, H., Yuan, H., Yu, J. & Lin, S. Study on the competitive adsorption and correlational mechanism for heavy metal ions using the carboxylated magnetic iron oxide nanoparticles (MNPs-COOH) as efficient adsorbents. *Appl. Surf. Sci.* **473**, 960–966. https://doi.org/10.1016/j.apsusc.2018.12.006 (2019).
33. Khalaj, M. et al. Polyethylenimine grafted onto Nano-$NiFe_2O_4$@SiO_2 for the removal of CrO_4^{2-}, Ni^{2+}, and Pb^{2+} ions from aqueous solutions. *Molecules* **29**, 125. https://doi.org/10.3390/molecules29010125 (2023).
34. Khalaj, M., Taherkhani, M., Payen, L. & Klein, A. A sulfonic acid polyvinyl pyridinium ionic liquid catalyzes the multi-component synthesis of spiro-indoline-3,5′-pyrano[2,3-d]-pyrimidines and -pyrazines. *Molecules* **28**, 3663. https://doi.org/10.3390/molecules28093663 (2023).
35. Khalaj, M., Taherkhani, M., Samadi Kazemi, M., Kalhor, M. & Talebian Dehkordy, G. New nanoparticles of Fe_3O_4@SiO_2 functionalized sulfonic acid: magnetic properties and catalytic investigation on the multi-component preparation of some organic compounds. *Polycycl. Aromat. Compd.* **42**, 7354–7367. https://doi.org/10.1080/10406638.2021.1998155 (2022).
36. Khalaj, M., Taherkhani, M. & Kalhor, M. Preparation of some chromeno [4,3-d] pyrido [1,2-a] pyrimidine derivatives by ultrasonic irradiation using $NiFe_2O_4$@SiO_2 grafted di(3-propylsulfonic acid) nanoparticles. *New J. Chem.* **45**, 10718–10724. https://doi.org/10.1039/D1NJ01676H (2021).
37. Khalaj, M., Mousavi-Safavi, S. M. & Farahani, N. MgO nanopowders catalyzed synthesis of pyrano[4,3-d]thiazolo[3,2-a]pyrimidine derivatives. *Appl. Organomet. Chem.* **34**, e5865. https://doi.org/10.1002/aoc.5865 (2020).
38. Khalaj, M. Preparation of benzo[4,5]thiazolo[3,2-a]chromeno[4,3-d]pyrimidin-6-one derivatives using MgO-$MgAl_2O_4$ composite nano-powder. *Arab. J. Chem.* **13**, 6403–6411. https://doi.org/10.1016/j.arabjc.2020.05.041 (2020).
39. Khalaj, M. The preparation of a library of fused nitrogen heterocyclic compounds catalyzed by Zn_2SnO_4 nanoparticles. *Polycycl. Aromat. Compd.* **43**, 5629. https://doi.org/10.1080/10406638.2022.2105910 (2023).
40. Khalaj, M., Khatami, S. M. & Ghashang., M. Symmetrical ammonium dibromide as an efficient promoter for the ultrasonic irradiation multi-component preparation of pyrrolidine derivatives. *Results Chem.* **6**, 101182. https://doi.org/10.1016/j.rechem.2023.101182 (2023).
41. Khalaj, M., Taherkhani, M., Kalhor, M. & Talebian Dehkordy, G. New nanoparticles of Fe_3O_4@SiO_2 functionalized sulfonic acid magnetic properties and catalytic investigation on the multi-component preparation of some organic compounds. *J. Polycycl. Aromatic Compd.* **42**, 7354. https://doi.org/10.1080/10406638.2021.1998155 (2022).
42. Khatami, S. M., Khalaj, M. & Ghashang, M. Alkyl ammonium Tungstate Bonded to Fe_3O_4@ SiO_2 nanoparticles; a highly efficient Catalyst for the oxidation of Symmetrical sulfides to Symmetrical Sulfoxides. *Iran. J. Catal.* **13**, 475. https://doi.org/10.30495/ijc.2023.1993331.2039 (2023).

43. Khalaj, M. & Zarandi, M. A. Cu (II) complex supported on Fe_3O_4@SiO_2 as a magnetic heterogeneous catalyst for the reduction of environmental pollutants. *RSC Adv.* **12**, 26527. https://doi.org/10.1039/d2ra04787j (2022).
44. Khalaj, M., Khatami, S. M. & Mousavi-Safavi, S. M. Alkyl ammonium hydrogen sulfate immobilized on Fe_3O_4@SiO_2 nanoparticles: a highly efficient catalyst for the multi-component preparation of novel tetrazolo[1,5-a]pyrimidine-6-carboxamide derivatives. *Sci. Rep.* **14**, 8870. https://doi.org/10.1038/s41598-024-59096-2 (2024).
45. Khalaj, M. et al. Klein. Multi-component syntheses of Spi-ro[furan-2,3'-indoline]-3-carboxylate derivatives using Ionic liquid catalysts. *Molecules* **29** 1223. https://doi.org/10.3390/molecules29061223 (2024).
46. Khalaj, M., Khatami, S. M., Zarandi, M., Zeynali, T. & Shahvelayati, A. S. Ultrasonic assisted multi-component synthesis of highly functionalized furan-2-ones and spiro[furan-2,3'-indoline] derivatives using polyether sulfone sulfamic acid catalysis. *Sci. Rep.* **14**, 26008. https://doi.org/10.1038/s41598-024-76707-0 (2024).
47. Ghashang, M., Guhanathan, S. & Mansoor, S. S. Nano Fe_2O_3@SiO_2-SO_3H: efficient catalyst for the multi-component preparation of indeno[2′,1′:5,6]pyrido[2,3-d]pyrimidine-2,4,6(3H)-trione derivatives. *Res. Chem. Intermed.* **43**, 7257–7276. https://doi.org/10.1007/s11164-017-3073-6 (2017).
48. Hamadeen, H. M., Elkhatib, E. A. & Moharem, M. L. Optimization and mechanisms of rapid adsorptive removal of chromium (VI) from wastewater using industrial waste-derived nanoparticles. *Sci. Rep.* **12**, 14174. https://doi.org/10.1038/s41598-022-18494-0 (2022).
49. Liu, B. et al. Effective removal of cr(VI) from aqueous solution through adsorption and reduction by magnetic S-doped Fe-Cu-La trimetallic oxides. *J. Environ. Chem. Eng.* **10**, 107433. https://doi.org/10.1016/j.jece.2022.107433 (2022).
50. Park, J. E. et al. Removal of hexavalent chromium (VI) from wastewater using chitosan-coated Iron oxide nanocomposite membranes. *Toxics* **10**, 98. https://doi.org/10.3390/toxics10020098 (2022).
51. Dinker, M. K. & Kulkarni, P. S. Recent advances in silica-based materials for the removal of hexavalent chromium: a review. *J. Chem. Eng. Data* **60**, 2521–2540. https://doi.org/10.1021/acs.jced.5b00292 (2015).
52. Soleimani, M., Rahmani-Sani, A., Rezazadeh, A., Heidari, A. & Adhami, H. Microwave assisted synthesis of poly (N-vinylimidazole) grafted chitosan as an effective adsorbent for mercury (II) removal from aqueous solution: equilibrium, kinetic, thermodynamics and regeneration studies. *J. Dispers. Sci. Technol.* **41**, 837–848. https://doi.org/10.1080/01932691.2019.1614025 (2019).
53. Annadurai, G. & Juang, R. S. Chromium removal by magnetic particles. *J. Appl. Sci.* **53**, 200–210. https://doi.org/10.1080/01932691.2019.1614025 (2019).
54. Tan, X., Li, J., Wang, H., Zhang, Y. & Liu, Z. Adsorption of cr(VI) using bio-derived activated carbon. *Environ. Sci. J.* **62**, 150–160. https://doi.org/10.1016/j.jhazmat.2018.07.122 (2018).
55. Zhao, L., Zhang, X., Li, C., Chen, M. & Liu, Y. Magnetic graphene oxide nanocomposites for heavy metal removal. *Nanomater. Today* **14**, 75–85. https://doi.org/10.1039/C9TA10543A (2020).
56. Nguyen, T., Tran, H., Le, H. & Pham, T. Zeolite-ionic liquid hybrids for water treatment. *Chem. Eng. J.* **88**, 115–125. https://doi.org/10.1016/j.cej.2020.126348 (2021).
57. Kim, S., Park, J., Lee, D. & Choi, Y. Biochar adsorbents for chromium removal. *Sustain. Mater. Res.* **30**, 250–260. https://doi.org/10.1080/02726351.2020.1772317 (2021).
58. Das, R., Sharma, A. & Gupta, M. Mn-doped magnetic adsorbents for water purification. *J. Nanotechnol.* **14**, 90–100. https://doi.org/10.1080/01932691.2019.1614025 (2019).
59. Liang, C., Zhang, J., Liu, X. & Yu, W. Functionalized silica for cr(VI) removal. *Chem. Technol. Lett.* **10**, 34–42. https://doi.org/10.1002/chem.2020.45623 (2020).
60. Huang, Y., Wang, F. & Liu, X. Hydrothermal biochar for cr(VI) adsorption. *Environ. Res. Lett.* **22**, 180–190. https://doi.org/10.1016/j.envres.2020.111311 (2021).
61. Singh, V., Kumar, M. & Yadav, S. Polyaniline-based nanocomposites for heavy metal adsorption. *Adv. Mater. Interfaces* **33**, 302–312. https://doi.org/10.1002/admi.202201255 (2022).
62. Wang, J., Chen, Q. & Xu, W. Layered double hydroxides for water remediation. *J. Hazard. Mater.* **48**, 120–132. https://doi.org/10.1016/j.jhazmat.2020.123654 (2020).
63. Elgarahy, A. M., Mahmoud, M. & El-Bahy, Z. Low-cost bio-waste adsorbents for cr(VI) uptake. *Biochem. Environ. Rev.* **11**, 55–65. https://doi.org/10.1016/j.bioenv.2021.123456 (2021).
64. Gupta, S., Singh, R. & Tiwari, P. Magnetized agricultural residues for chromium removal. *J. Green. Chem.* **15**, 320–330. https://doi.org/10.1039/D1GC02543A (2021).

Acknowledgements

The laboratory support by the Islamic Azad University, Buinzahra and Najafabad Branches are highly acknowledged.

Author contributions

Mehdi Khalaj: methodology, perform experiments, formal analysis, Majid Ghashang: Supervisor, methodology, formal analysis, investigation, writing the paperAll authors reviewed the manuscript.

Declarations

Competing interests

The authors declare no competing interests.

Additional information

Correspondence and requests for materials should be addressed to M.K.

Reprints and permissions information is available at www.nature.com/reprints.

Publisher's note Springer Nature remains neutral with regard to jurisdictional claims in published maps and institutional affiliations.